Identification of Excitons and Biexcitons in Sb_2Se_3 under High Photoluminescence Excitation Density

Jüri Krustok,* Rokas Kondrotas, Ramunas Nedzinskas, Kristi Timmo, Reelika Kaupmees, Valdek Mikli, and Maarja Grossberg

The near-band-edge emission of Sb_2Se_3 microcrystals is studied in detail under high photoluminescence excitation density using a pulsed UV laser ($\lambda = 266$ nm, pulse width 0.6 ns). Based on the peak energy positions and the excitation power density and temperature dependencies ($T = 3$–110 K) of the photoluminescence spectra, the emission is interpreted as a recombination of two pairs (A and B) of free excitons and biexcitons appearing because of valence band splitting. The magnitude of the valence band splitting due to the crystal field ($\Delta_{cr} = 20$–22 meV) is estimated in the Brillouin zone center. At $T = 3$ K, the A and B biexciton emission at 1.302 and 1.322 eV, respectively, and the A and B free exciton emission at 1.311 and 1.333 eV, respectively, are observed. The binding energy of A and B biexcitons is 9 and 11 meV, respectively, and the binding energy of A free exciton is 6 meV. The activation energy of thermal quenching for all observed peaks is 20 meV.

1. Introduction

Development of photovoltaic (PV) materials consisting of earth abundant elements is an ultimate criterion to meet the increasing demands for electricity production. The current thin-film PV technologies are mostly dominated by two favorable compounds, i.e., CdTe and Cu(In,Ga)Se₂ (CIGS).[1,2] However, the high price of In and Ga as well as the toxicity of Cd may limit their widespread use. Alternative quaternary $Cu_2ZnSn(S,Se)_4$ (CZTSSe) type compounds, comprising abundant and low-cost elements like Cu, Zn, Sn, S, and Se, are also potential candidates for next-generation PV technologies.[3,4] However, kesterites have turned out to be very challenging on their way toward highly efficient thin film PV due to strong recombination of photogenerated charge carriers via various routes leading to short minority carrier lifetime (i.e., magnitude lower than in CIGS, CdTe, etc.) and diffusion length and resulting in large open circuit voltage deficit of kesterite solar cells.[3,5–8] It is, therefore, obvious that more research is required to find the alternative inexpensive and earth abundant materials for efficient thin-film solar cells. One of the promising absorber material candidates among the inorganic semiconductors being in the spotlight these days is antimony triselenide (Sb_2Se_3). The efficiencies of the corresponding thin-film solar cells have already boosted to 9.2% in a very short time.[9–11] Quasi-1D antimony triselenide belongs to a family of inorganic binary $A^V–B^{VI}$ compounds and indeed has very attractive properties, such as proper optical bandgap (1.1–1.2 eV) for a solar absorber, a single phase structure, high light absorption coefficient (10^5 cm^{-1}), low toxicity, and high element abundance.[12] It was shown that due to the very high absorption coefficient the photons with wavelengths $\lambda > 800$ nm are completely absorbed within the first 400 nm of Sb_2Se_3 film, enabling much thinner absorber layers compared to the usual thin film solar cells.[13] Despite extensive research there are still problems related to various point defects or electronic band structure of this compound. Capacitance spectroscopy studies have shown the presence of various deep donor and acceptor defects.[14,15] Defect states in polycrystalline Sb_2Se_3 have been studied also using temperature and laser intensity-dependent photoluminescence (PL).[16] The low-temperature ($T = 10$ K) PL spectrum was consisted of three bands at 0.94, 1.10, and 1.24 eV. The PL bands at 1.24 and 0.94 eV were found to originate from the distant and close donor–acceptor pair recombination, respectively, and the third PL band at 1.10 eV was proposed to be related to the grain boundaries. Recent theoretical calculations showed that the defect chemistry of quasi-1D Sb_2Se_3 is rather complicated compared to conventional semiconductors. In particular, it has been discussed that the identical defects located on nonequivalent atomic sites might have different properties.[17] All kinds of defect studies are therefore extremely important as usually defects act as powerful recombination channels and reduce the performance of the solar cell.

Prof. J. Krustok
Division of Physics
Tallinn University of Technology
Ehitajate Tee 5, Tallinn 19086, Estonia
E-mail: Juri.Krustok@ttu.ee

Prof. J. Krustok, Dr. K. Timmo, R. Kaupmees, Dr. V. Mikli,
Prof. M. Grossberg
Department of Materials and Environmental Technology
Tallinn University of Technology
Ehitajate Tee 5, Tallinn 19086, Estonia

Dr. R. Kondrotas, Dr. R. Nedzinskas
State Research Institute
Center for Physical Sciences and Technology
Savanorių Ave. 231, Vilnius 02300, Lithuania

Besides the complicated defect structure, the electronic band structure of Sb_2Se_3 is also not fully understood. There are contradictory reports regarding the nature of the band gap (direct/indirect), as well as a significant range of values for its energy. There now exists a broad consensus that the band structure and optical properties of Sb_2Se_3 strongly depend on both, crystal structure and small deviation from ideal stoichiometry. This is why thin films prepared by various methods and growth conditions could have different Sb/Se ratios and/or different crystalline quality and properties. The fundamental band gap of Sb_2Se_3 at room temperature (RT) is generally considered to be indirect with a direct gap lying at ≈0.1 eV to higher energy.[13] Moreover, the temperature dependence of indirect and direct band gaps is different and therefore the energy difference between them is found to be only about 40 meV at $T = 0$ K.[13] At the same time, a slightly smaller difference of about 25 meV at $T = 0$ K was also reported.[18] In most of the studies, absorption measurements and Tauc's plot are used to determine the bandgap energy, but it is extremely difficult to distinguish between so closely situated indirect and direct band gaps with this method. Moreover, the absorption spectrum is often disturbed by the Urbach tail.[13,19] Photoreflectance spectroscopy (PR) is considered to be more reliable method, but unfortunately this technique probes exclusively direct optical transitions that are present at singularities of the joint optical density of states. According to PR measurements made on polycrystalline samples, the bandgap energy at $T = 0$ K was around 1.32 eV.[16,18] There is less information about band structure of single-crystalline Sb_2Se_3 samples. Recent optical measurements made on quasi-1D Sb_2Se_3 single crystals revealed that the absorption edge at low temperatures can shift about 10 meV depending on polarization conditions and even more at RT.[20] This anisotropy affects also the shape of absorption spectrum and could cause additional ambiguity to experimental results. Additionally, the valence band splitting in the center of the Brillouin zone by a crystal field and the spin–orbit interaction add extra features to the optical absorption and reflectance measurements. Unfortunately, PR measurements were not able to detect these valence band splittings, because the broadening parameter obtained from PR spectra was too high. Very recently, the presence of four different excitonic transitions was reported by using absorption and reflectance measurements at $T = 11$ K and at $T = 300$ K.[20] These transitions are due to the crystal field (Δ_{cr}) and spin–orbit (Δ_{so}) interactions leading to valence band splitting in the center of the Brillouin zone center and are called as A, B, C, and D excitons. The low-temperature ground state energy positions of these excitons were measured at 1.299, 1.312, 1.347, and 1.538 eV for A, B, C, and D excitons, respectively. Due to crystal symmetry rules, A exciton is allowed in $E\|c$ polarization while the B exciton in $E\perp c$ polarization. It was additionally shown in Sb_2Se_3 single crystals $\Delta_{cr} = 13$ meV and $\Delta_{so} = 35$ meV.[20] All these aforementioned results show that additional methods are also needed to improve the understanding of the electronic band structure of Sb_2Se_3 crystals in more detail.

Excitons are most often studied by low-temperature PL spectroscopy, which, however, requires very high-quality crystals, where other recombination channels are suppressed. Alternatively, it is possible to dramatically increase the probability of free exciton emission by the generation of very high concentration of electron–hole pairs.[21] This can be done by using very high laser power. However, when continuous wave (cw) laser is used, there is a high risk of overheating the crystal before reaching the required power. Therefore, pulsed lasers with very short laser pulses must be used.[22] It was estimated that a pulsed laser can produce 15 times more excitons and about 150 times more biexcitons than cw excitation under the same experimental conditions.[23] There are also requirements for the laser wavelength. It should be as short as possible in order to increase the density of generated free excitons. In Sb_2Se_3, the absorption coefficient at $\lambda < 400$ nm is reaching 10^6 cm^{-1} and the electron–hole pairs are generated in a thin surface layer with a thickness of only a few tens of nanometers.[13] In the present paper, we report the first detection of excitonic emission in Sb_2Se_3 microcrystals by using pulsed UV laser and analyze the properties of detected A and B free excitons and biexcitons.

2. Excitons and Biexcitons

The free exciton binding energy in 3D crystals is usually calculated using a simple hydrogen model[24]

$$E_b = \frac{\mu R_y}{m_0 \varepsilon_r^2} \quad (1)$$

where $\mu = (m_e^* m_h^*)/(m_e^* + m_h^*)$ is the reduced mass of exciton, m_0 is the electron mass, and R_y is the Rydberg constant. Sb_2Se_3 is a compound with quite high static permittivity, i.e., $\varepsilon_r \geq 24$[20,25] and therefore the free exciton binding energy is expected to be very small. As already mentioned, due to the crystal field splitting of valence band we expect at least the presence of A and B excitons in this material.[26] Effective mass of electrons in Sb_2Se_3 is reported to be $m_e^* = 0.67m_0$ and the effective mass of holes in the upper valence bands A and B is $m_h^* = 3.32m_0$ and $m_h^* = 3.83m_0$, respectively.[20] However, different values of electron and hole effective masses were also reported: $m_e^* = 0.365m_0$ and $m_h^* = 0.316m_0$;[27] $m_e^* = 0.42m_0$ and $m_h^* = 0.31m_0$.[28] These values give the free exciton binding energy in the range of $E_{bA} = 4$–9 meV and the exciton radius is about 7 nm. The separation between A and B excitons in Sb_2Se_3 at low temperature is expected to be $\Delta_{cr} = 13$ meV.[20] It is also known that Sb_2Se_3 is a semiconductor with a layered structure in which the Sb and Se atoms are connected with three other atoms of the opposite type, which in turn are connected within the crystal through weak secondary bonds. It was shown that the free exciton binding energy in layered crystals can be higher than in ordinary 3D crystals.[29]

First studies of biexcitons were made using CuCl crystals, see ref. [30] and references therein. It was discovered that the properties of biexciton emission are very different from free exciton emission. First, the integral intensity of biexciton emission Φ_{XX} shows a superlinear growth with the increase in excitation intensity L while the integral intensity of free exciton emission Φ_X is growing linearly. The experimental data can usually be fitted by the simple power law of the form $\Phi \propto L^m$, where $m \approx 1$ and $m \approx 2$ for free excitons and biexcitons, respectively.[31,32] Therefore, at higher laser, power biexciton emission
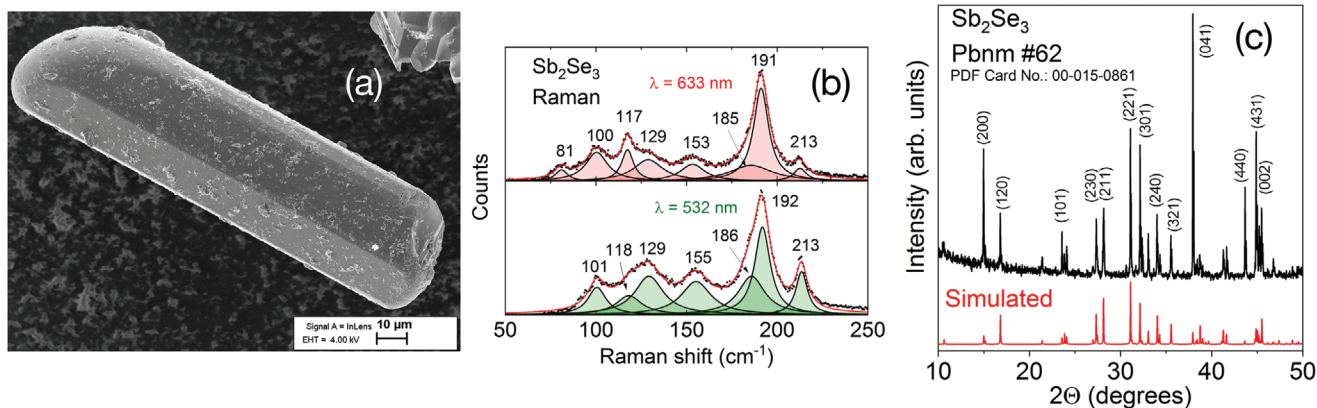
Figure 1. a) SEM image of a typical Sb$_2$Se$_3$ needle-like microcrystal. b) RT Raman spectra of Sb$_2$Se$_3$ microcrystals. Result of fitting with Lorentzian curves is shown as solid lines. Experimental data are presented as black dots. Laser excitation wavelength: $\lambda = 633$ nm (upper graph) and $\lambda = 532$ nm (lower graph). c) The XRD pattern of the studied Sb$_2$Se$_3$ microcrystals and the simulated pattern according to the *Pbnm* #62 space group.

is typically dominating. Another difference of free exciton and biexciton properties is related to the temperature dependence of the peak position. Free exciton emission usually follows the temperature dependence of the bandgap energy while the biexciton peak position is showing more rapid redshift.[33] The biexciton emission happens by the radiative annihilation of biexciton into a free exciton and a photon. In this process, the momentum and energy conservation laws must be fulfilled[30,34]

$$K_{XX} = K_X \tag{2}$$

$$\left(2E_X - E_{XX}^b\right) - \frac{\hbar^2 K_{XX}^2}{2M_{XX}} = h\nu + E_X + \frac{\hbar^2 K_X^2}{2M_X} \tag{3}$$

here E_X and E_{XX}^b are the energy of ground state of free exciton and the binding energy of biexciton, respectively; K_X (K_{XX}) is the free exciton (biexciton) momentum, $h\nu$ is the energy of emitted photon, and M_X (M_{XX}) is the exciton (biexciton) effective mass. In the simplest case, $M_X = m_e^* + m_h^*$ and $M_{XX} = 2(m_e^* + m_h^*)$. Usually the momentum of the photon is neglected. Due to the preservation of momentum, free exciton emission occurs only from the recombination of free excitons with a momentum close to zero or with very low kinetic energy. In other words, high-momentum free excitons must relax through radiating phonons to reach the free excitonic states near the zone center from which the emission may occur. Specifically, free excitons acquired high kinetic energy (high K_X) at higher temperatures from states that could not emit photons without phonon assistance, while biexcitons were able to recombine at high kinetic energy (high K_{XX}) states to radiate photons and free excitons as well. Of course, the excess energy must be carried by the remaining free excitons. Therefore, we can neglect the kinetic energy of excitons and calculate the photon energy emitted by biexcitons

$$h\nu = E_X - E_{XX}^b - \frac{\hbar^2 K_{XX}^2}{2M_{XX}} \tag{4}$$

where the last term is a kinetic energy of biexciton. The increasing lattice temperature increases also the kinetic
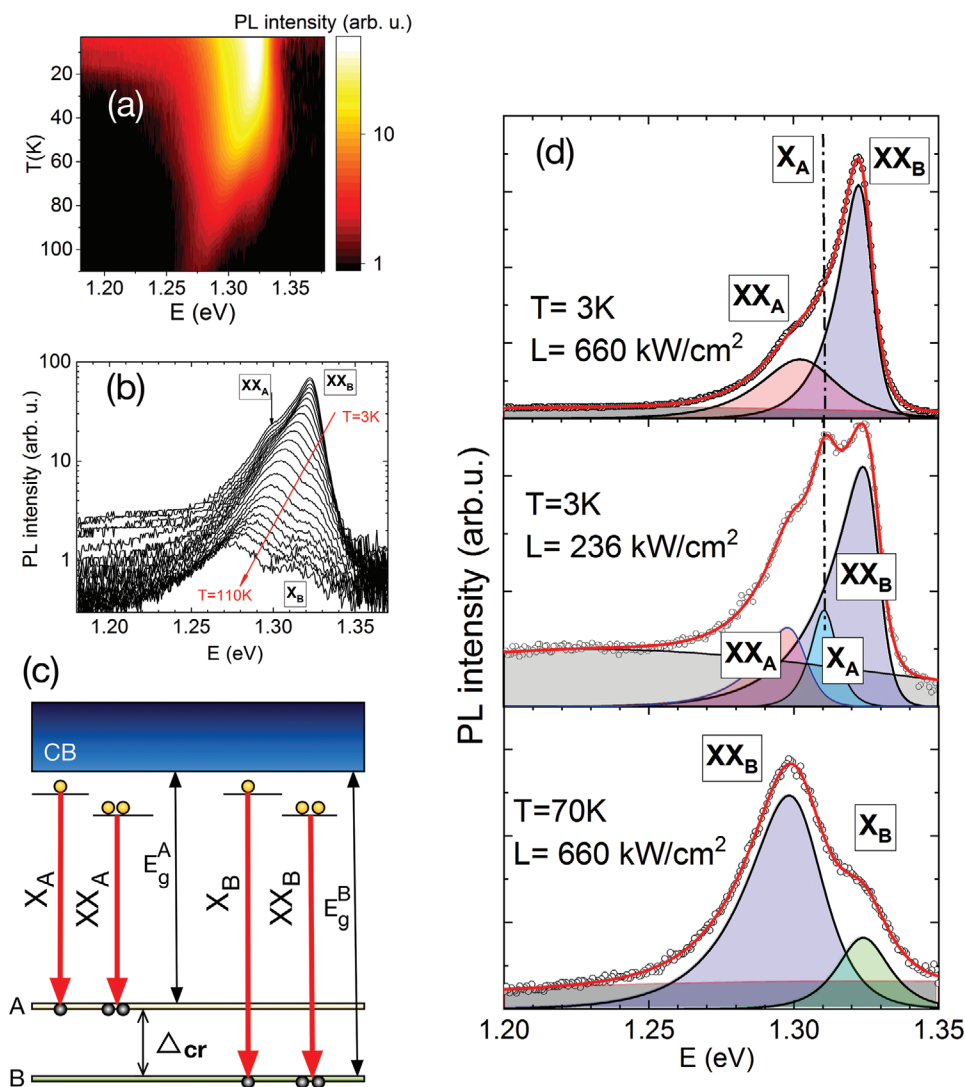
energy of biexcitons and thus the energy separation between free exciton and biexciton peak positions constantly increases with temperature. This effect was observed also in ZnS single crystals.[33] In principle, this energy separation must follow the statistic law of lattice heat energy, which is related to the phonon distributions in the crystal.

3. Results and Discussion

At first, we measured PL of three different Sb$_2$Se$_3$ samples: microcrystals grown at Se source temperatures of 450 and 380 °C and a bigger single crystal, see Figure S2 in the Supporting Information. All samples show very similar PL spectra, but the most intense emission and the lowest low energy tail we got from sample grown at Se source temperature of 450 °C, see Figure S2a in the Supporting Information. Therefore, all additional measurements were done using these microcrystals. We also measured deeper PL bands for this sample using continuous wave (cw) helium cadmium (HeCd) laser with a wavelength of 442 nm and power of 37.1 mW. The resulting spectrum was very similar to the PL spectrum of Sb$_2$Se$_3$ polycrystals,[16] see Figure S3 in the Supporting Information. No exciton emission was detected using cw excitation.

The Sb$_2$Se$_3$ sample for PL measurements consisted of several dozen randomly oriented microcrystals. Most of these microcrystals had a needle-like shape with flat well-formed facets, see **Figure 1**a and Figure S1a in the Supporting Information.

Figure 1b presents a deconvoluted Raman spectra of Sb$_2$Se$_3$ microcrystals fitted using Lorentzian function to resolve the peaks. Spectra were measured at RT using two different lasers. It can be seen that by using red laser ($\lambda = 633$ nm) we were able to reveal also a peak at 81 cm^{-1}. All observed peaks belong to Sb$_2$Se$_3$ and were found and theoretically predicted also in refs. [16,35–37]. The X-ray diffraction (XRD) pattern of the studied Sb$_2$Se$_3$ microcrystals is presented in Figure 1c. According to the XRD analysis, the material crystallizes in orthorhombic structure of Sb$_2$Se$_3$ with space group *Pbnm* #62. All detected XRD peaks belong to Sb$_2$Se$_3$. According to the peak positions, estimated lattice parameters are: $a = 1.1784$ nm,

ADVANCED
SCIENCE NEWS
www.advancedsciencenews.com

ADVANCED
OPTICAL
MATERIALS
www.advopticalmat.de

Figure 2. a) Color-filled 2D topographical map of Sb_2Se_3 PL at different temperatures, b) the temperature dependence of the PL spectrum of the studied Sb_2Se_3 microcrystals measured with laser peak power density 660 kW cm^{-2}, c) model of detected free exciton and biexciton peaks, d) results of spectral fitting of Sb_2Se_3 microcrystals edge emission at different temperatures and laser powers using the asymmetric hyperbolic secant function.

$b = 0.3980$ nm, and $c = 1.1650$ nm. These values are in good agreement with the values found in literature and in crystallographic database.[16,38] **Figure 2**a,b illustrates the PL spectra of Sb_2Se_3 microcrystals at different temperatures, measured with laser peak power density of 660 kW cm^{-2} ($\lambda = 266$ nm). At $T = 3$ K, only two slightly asymmetric biexciton peaks can be detected labeled as XX_B and XX_A, but with increasing the temperature the XX_B peak vanishes and a new peak X_B appears at higher photon energy. All these peaks show a redshift with increasing temperature.

For spectral fitting of PL peaks, we used an asymmetric hyperbolic secant function

$$I = \frac{I_0}{\exp\left[(E - E_0) / W_H\right] + \exp\left[-(E - E_0) / W_L\right]} \quad (5)$$

where I is the PL intensity, I_0 is a parameter related to the maximum intensity of the PL peak, E_0 is a parameter which

is related to the peak position of the PL peak, E is a photon energy, W_L and W_H are parameters related to the peak width from low and high energy side of the peak, respectively. This fitting function was successfully used in slightly disordered 2D materials, where exciton and trion peaks were weakly asymmetric.[39,40] For all peaks $W_L > W_H$. Theoretical calculations also have shown that the shape of biexciton peak is asymmetric, but the actual shape is still not completely settled.[34] All PL spectra were showing also a wide background at lower photon energies and this background was fitted using Gaussian shape. Results of these spectral fittings are given in Figure 2d.

The full-width at half-maximum (FWHM) of the peaks at $T = 3$ K is in the range of 10–30 meV. This rather small width is typical for PL peaks having excitonic origin. Additional peak X_A becomes more apparent, when the laser power was reduced, see Figure 2d and **Figure 3**c. The model of detected free exciton and biexciton peaks is presented in Figure 2c and peak positions are given in **Table 1**.
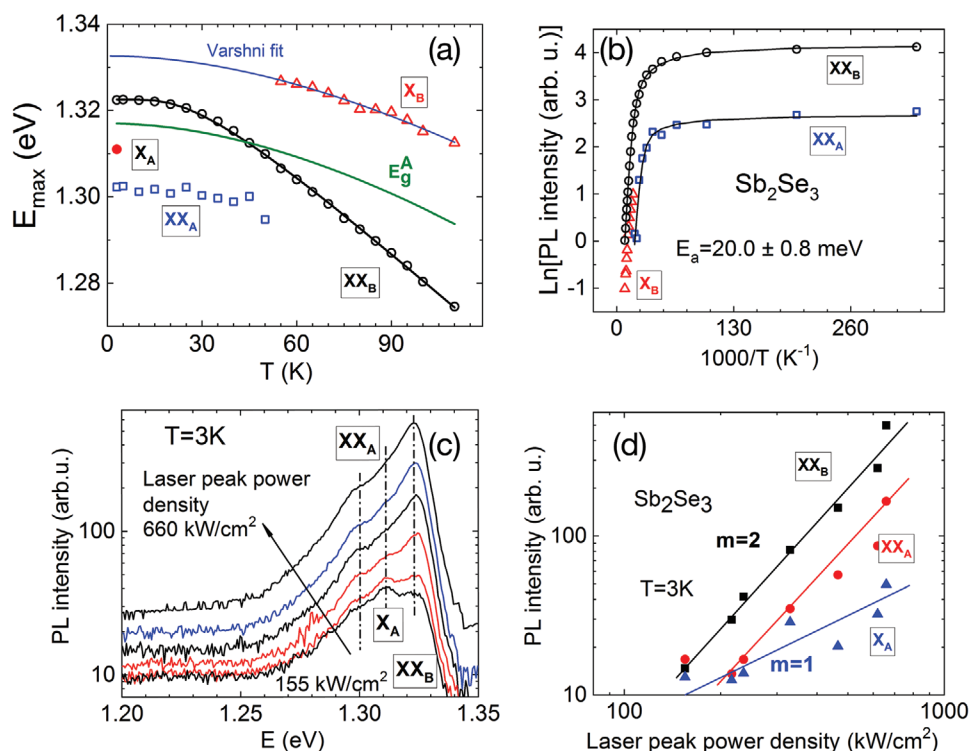
Figure 3. a) Temperature dependence of the peak position of the free-excitonic (X) and biexcitonic (XX) emissions in Sb_2Se_3 microcrystals measured with laser peak power density $L = 660$ kW cm^{-2}. Temperature dependence of E_g^A measured by photoreflectance[16,18] is given as a green line, the X_B peak was fitted using Varshni expression (blue line), the black line for XX_B peak position is just a guide to the eye. b) PL intensities of the free-excitonic and biexcitonic transitions as a function of reverse temperature. Dots are experimental data. Lines are the fits with Equation (6). c) PL spectra of Sb_2Se_3 microcrystals at $T = 3$ K measured at different average laser power. d) Excitation power density dependence of the free exciton and biexcitons PL intensity in Sb_2Se_3 microcrystals at $T = 3$ K.

In Figure 3a, the peak positions of the free exciton X_B and biexcitons XX_B and XX_A depending on the sample temperature are shown. The peak position of X_A free exciton is given at $T = 3$ K as a red dot. The temperature dependence of the X_B peak position was fitted with the empirical Varshni expression[41] $E_{max} = E_0 - \alpha T^2/(\beta + T)$, where E_0 is the zero Kelvin peak position. The Varshni parameters E_0, α, and β determined for X_B are, respectively, 1.333 eV, 0.77 meV K^{-1}, and 354 K. The same expression was used also for E_g^A,[18] where obtained parameters were 1.317 eV, 0.90 meV K^{-1}, and 358 K. The temperature dependence of E_g^A is given as a green line in Figure 3a. The slight difference of parameters α and β for the X_B peak position and E_g^A is mostly related to small difference between temperature dependence of E_g^A and E_g^B, because the free exciton peak usually follows the temperature dependence of bandgap energy. At the same time, the temperature dependence of XX_B

peak position shows more noticeable redshift and this is typical for biexciton peak position. Unfortunately, the intensity of the XX_A peak dropped rapidly with temperature and we could not determine the behavior of this peak at higher temperatures, where this peak is expected to show similar to XX_B temperature dependence. According to these obtained values of peak positions, the value of the crystal field splitting is $\Delta_{cr} = 20$–22 meV. This is slightly higher than the value obtained from absorption measurements in ref. [20].

Next, the analysis of the temperature quenching of the PL peaks was carried out, see Figure 3b. An Arrhenius plot of the resulting integral intensity was fitted using a model of a single recombination channel proposed in ref. [42]

$$\Phi(T) = \Phi_0 / \left[1 + \alpha_1 T^{3/2} + \alpha_2 T^{3/2} \exp(-E_a/kT) \right] \quad (6)$$

where Φ_0 is the integral intensity of the PL peaks at 0 K, α_1 and α_2 are process rate parameters, and E_a is the activation energy. It turned out that all peaks show quite similar thermal quenching activation energy $E_a = 20.0 \pm 0.8$ meV, but parameters α_1 and α_2 were different for different peaks. At low excitation density, the quenching process of biexciton emission is mainly due to the thermal dissociation of biexciton into free excitons while the temperature quenching of excitonic lines is due to the thermally activated depopulation of the free excitonic level and/or to the activation of nonradiative recombination centers. The similar thermal activation energy for free

Table 1. Detailed features and transition assignments of the near-band-edge PL peaks in Sb_2Se_3 microcrystals. Calculated binding energies are given in the last column.

Peak label	Peak position at $T = 3$ K [eV]	Assignments	Binding energy [meV]
X_B	1.333 (estimated)	Free exciton (B)	–
XX_B	1.322	Biexciton (B)	11
X_A	1.311	Free exciton (A)	6
XX_A	1.302	Biexciton (A)	9

ADVANCED
SCIENCE NEWS
www.advancedsciencenews.com

ADVANCED
OPTICAL
MATERIALS
www.advopticalmat.de

exciton and biexciton peaks exceeding about twice the binding energies is probably an indication of nonradiative processes at high excitation density. At higher temperatures, the generation rate of biexcitons and free excitons is quite high and despite increasing thermal dissociation the concentration of both exciton features is notable. However, the role of the exciton–phonon and exciton–exciton scattering is increasing with temperature and thus the overall intensity of PL peaks starts to decrease. High thermal activation energy of exciton emission exceeding the exciton or biexciton binding energy was also found in MAPbBr$_3$ perovskite quantum dots[43] and in CuInSe$_2$.[26] It was concluded that the usual dissociation of free excitons or biexcitons into the continuum states and trapping by the nonradiative centers cannot be the only process leading to the thermal quenching of PL. However, additional studies are needed to specify the mechanism of thermal quenching of these PL peaks.

Additional proof of free exciton and biexciton emission can be found from laser power dependence of our PL peaks. By decreasing the laser power, we did not notice any shift of peak position of all PL peaks and the X$_A$ PL peak is more exposed at lower laser power, see Figure 3c. The integral intensity dependence of PL peaks on laser power is presented in Figure 3d. As predicted by theory, both biexciton peaks (XX$_A$ and XX$_B$) show superlinear growth with $m = 2$ while the intensity of free exciton peak (X$_A$) increases linearly with $m \approx 1$.

According to peak position of observed free exciton and biexciton peaks at $T = 3$ K, we calculated also the binding energies, see Table 1. The binding energy for the X$_B$ free exciton was not determined, because we do not have definite value for E_g^B. However, we believe that the binding energy is very close to the value of X$_A$ binding energy. Unfortunately, we were not able to detect any sign of indirect transitions predicted by other groups. Apparently, other methods are needed to uncover indirect transitions in Sb$_2$Se$_3$.

4. Conclusions

In conclusion, we present a detailed study of free exciton and biexciton emissions in Sb$_2$Se$_3$ microcrystals. Due to the crystal field splitting of the valence band ($\Delta_{cr} = 20$–22 meV), we observed two different free exciton PL peaks and two different biexciton peaks at $T = 3$ K: X$_A$, X$_B$, XX$_A$, and XX$_B$ centered at 1.311, 1.333, 1.302, and 1.322 eV, respectively. The binding energy of biexcitons was 9 and 11 meV for A and B biexcitons, respectively. Both biexciton peaks (XX$_A$ and XX$_B$) show a superlinear growth while the intensity of free exciton peak (X$_A$) increases linearly on laser power. The temperature dependence of XX$_B$ peak position shows noticeable redshift typical for biexciton peak position. This shift is faster than the normal temperature shift caused by the temperature dependence of the bandgap energy. The fast shift with temperature is attributed to the contribution of the biexcitonic kinetic energy. We also found that all PL peaks show quite similar thermal quenching activation energy $E_a = 20.0 \pm 0.8$ meV and this is probably related to the activation of common nonradiative recombination channel.

5. Experimental Section

The Sb$_2$Se$_3$ microcrystalline powder was synthesized in a two-temperature zone furnace in a sealed evacuated quartz ampoule from Sb metal powder (5N, −200 mesh powder, Alfa Aesar) and elemental Se pellets (4N purity). 0.1 g Sb metal powder was poured into one side of a quartz ampoule by using polymer funnel and as a chalcogen source 0.118 g Se pellets were introduced in the other side. The volume of used ampoule was ≈25 mL with inside diameter of 1.0 cm and length of 32.5 cm. The precursors inside the ampoule were degassed under dynamic (continuous) vacuum-pumping process for 1 h at RT and the ampoule was sealed at a vacuum level of 1.3×10^{-2} mbar (0.01 torr). Sealing was done by using O$_2$ + propane flame. After that, sealed ampoule was placed into a pre-heated two-zone tube furnace, where the temperature of both zones was controlled and regulated precisely. In such an arrangement, the vapor pressure of the Se source was determined and controlled by the lowest temperature in the system. The temperature zone in which the Sb powder was located was kept at 500 °C and the Se source temperature was kept at 450 °C, which corresponds to the partial pressure of Se of 16.4 mbar (≈12.3 torr). Additionally, a second growth was also made with a Se source temperature of 380 °C corresponding to the Se pressure of 2.67 mbar (≈2 torr). The formation process of Sb$_2$Se$_3$ took place at these temperature regimes for 96 h. Finally, the ampoule was taken out from the furnace with the Se source side ahead and cooled down to RT with a cooling rate of 120 °C min^{-1}. The obtained Sb$_2$Se$_3$ microcrystalline powder contained well-formed monocrystalline needles with flat and shiny facets and additionally some polycrystalline fragments of Sb$_2$Se$_3$. At disposal, a bigger single crystal made by liquid-phase epitaxy (LPE) was seen, see Figure S1b,c in the Supporting Information.

XRD patterns were recorded using Smartlab (Rigaku) diffractometer equipped with rotating 9 kW Cu anode X-ray tube. Powder sample was measured in Bragg-Brentano geometry in 10°–70° 2θ angle range with 0.02° step. Reference XRD pattern was simulated from Sb$_2$Se$_3$ CIF file obtained from crystallographic open database. Lattice parameters were calculated manually to match experimental XRD peak positions based on orthorhombic crystal system.

The shape and surface morphology of the synthesized microcrystals were studied with a high-resolution scanning electron microscope (SEM), Zeiss MERLIN.

For the PL excitation, a diode pumped Nd:YAG solid state 266 nm laser was used with the pulse width 0.6 ns and repetition rate 19 kHz. The maximum peak energy was 0.75 µJ and the maximum average power was 7.15 mW. The maximum peak power density was estimated to be 660 kW cm^{-2}. The laser beam was not focused to avoid damaging the sample and the pump power was reduced by a gradient UV (fused silica) filter.

PL was dispersed by using the 500 mm focal length monochromator (Andor SR-500i; grating 600 g mm^{-1} blazing at 1000 nm) and focused into thermoelectrically cooled InGaAs photodetector (IGA-030-TE2-H; Electro-Optical Systems Inc.). The conventional lock-in detection system (SR830; Stanford Research Systems) was used to extract the emission signal. The PL measurements were carried out in the temperature range of 3–110 K by mounting the samples (several dozen randomly oriented microcrystals) on the cold finger of a closed-cycle helium cryostat (Janis SHI-4; Lake Shore Cryotronics, Inc.).

Raman measurements were carried out using a Horiba LabRAM HR800 µ-Raman system equipped with a cooled multichannel CCD detection system in the backscattering configuration with a spectral resolution better than 1 cm^{-1}. A He-Ne laser (wavelength $\lambda = 633$ nm) and Nd:YAG laser (wavelength $\lambda = 532$ nm) were used for excitation. The laser spot size was about 5 µm in diameter.

Supporting information for additional SEM images of synthesized Sb$_2$Se$_3$, representative PL spectra of different samples, and deep PL is available from the Wiley Online Library or from the author.

Supporting Information

Supporting Information is available from the Wiley Online Library or from the author.

Acknowledgements

Conflict of Interest

The authors declare no conflict of interest.

Data Availability Statement

The data that support the findings of this study are available from the corresponding author upon reasonable request.

Keywords

[1] J. Ramanujam, U. P. Singh, *Energy Environ. Sci.* **2017**, *10*, 1306.
[2] T. Sinha, D. Lilhare, A. Khare, *J. Mater. Sci.* **2019**, *54*, 12189.
[3] S. Giraldo, Z. Jehl, M. Placidi, V. Izquierdo-Roca, A. Pérez-Rodríguez, E. Saucedo, *Adv. Mater.* **2019**, *31*, 1806692.
[4] A. Drabavičius, A. Naujokaitis, G. Stalnionis, R. Giraitis, Z. Mockus, S. Kanapeckaitė, P. Kalinauskas, R. Nedzinskas, G. Niaura, R. Juškėnas, *J. Alloys Compd.* **2020**, *824*, 153853.
[5] S. Kim, J. S. Park, A. Walsh, *ACS Energy Lett.* **2018**, *3*, 496.
[6] T. Ratz, G. Brammertz, R. Caballero, M. León, S. Canulescu, J. Schou, L. Gütay, D. Pareek, T. Taskesen, D.-H. Kim, J.-K. Kang, C. Malerba, A. Redinger, E. Saucedo, B. Shin, H. Tampo, K. Timmo, N. D. Nguyen, B. Vermang, *JPhys Energy* **2019**, *1*, 042003.
[7] M. Grossberg, J. Krustok, C. J. Hages, D. M. Bishop, O. Gunawan, R. Scheer, S. M. Lyam, H. Hempel, S. Levcenco, T. Unold, *JPhys Energy* **2019**, *1*, 044002.
[8] S. Bourdais, C. Choné, B. Delatouche, A. Jacob, G. Larramona, C. Moisan, A. Lafond, F. Donatini, G. Rey, S. Siebentritt, A. Walsh, G. Dennler, *Adv. Energy Mater.* **2016**, *6*, 1502276.
[9] K. Zeng, D. Xue, J. Tang, *Semicond. Sci. Technol.* **2016**, *31*, 063001.
[10] A. Mavlonov, T. Razykov, F. Raziq, J. Gan, J. Chantana, Y. Kawano, T. Nishimura, H. Wei, A. Zakutayev, T. Minemoto, X. Zu, S. Li, L. Qiao, *Sol. Energy* **2020**, *201*, 227.
[11] Z. Li, X. Liang, G. Li, H. Liu, H. Zhang, J. Guo, J. Chen, K. Shen, X. San, W. Yu, R. E. I. Schropp, Y. Mai, *Nat. Commun.* **2019**, *10*, 125.
[12] X. Wang, R. Tang, C. Wu, C. Zhu, T. Chen, *J. Energy Chem.* **2018**, *27*, 713.
[13] C. Chen, W. Li, Y. Zhou, C. Chen, M. Luo, X. Liu, K. Zeng, B. Yang, C. Zhang, J. Han, J. Tang, *Appl. Phys. Lett.* **2015**, *107*, 043905.
[14] X. Wen, C. Chen, S. Lu, K. Li, R. Kondrotas, Y. Zhao, W. Chen, L. Gao, C. Wang, J. Zhang, G. Niu, J. Tang, *Nat. Commun.* **2018**, *9*, 2179.
[15] J. Tao, X. Hu, J. Xue, Y. Wang, G. Weng, S. Chen, Z. Zhu, J. Chu, *Sol. Energy Mater. Sol. Cells* **2019**, *197*, 1.
[16] M. Grossberg, O. Volobujeva, A. Penežko, R. Kaupmees, T. Raadik, J. Krustok, *J. Alloys Compd.* **2020**, *817*, 152716.
[17] M. Huang, P. Xu, D. Han, J. Tang, S. Chen, *ACS Appl. Mater. Interfaces* **2019**, *11*, 15564.
[18] M. Birkett, W. M. Linhart, J. Stoner, L. J. Phillips, K. Durose, J. Alaria, J. D. Major, R. Kudrawiec, T. D. Veal, *APL Mater.* **2018**, *6*, 084901.
[19] S. Ghosh, M. V. B. Moreira, C. Fantini, J. C. González, *Sol. Energy* **2020**, *211*, 613.
[20] N. N. Syrbu, V. V. Zalamai, I. G. Stamov, S. I. Beril, *Beilstein J. Nanotechnol.* **2020**, *11*, 1045.
[21] C. H. Chia, Y. J. Lai, T. C. Han, J. W. Chiou, Y. M. Hu, W. C. Chou, *Appl. Phys. Lett.* **2010**, *96*, 081903.
[22] R. A. R. Leute, M. Feneberg, R. Sauer, K. Thonke, S. B. Thapa, F. Scholz, Y. Taniyasu, M. Kasu, *Appl. Phys. Lett.* **2009**, *95*, 031903.
[23] J. A. Smyder, A. R. Amori, M. Y. Odoi, H. A. Stern, J. J. Peterson, T. D. Krauss, *Phys. Chem. Chem. Phys.* **2014**, *16*, 25723.
[24] K. W. Böer, U. W. Pohl, in *Semiconductor Physics*, Springer International Publishing, Cham **2018**, pp. 485–525.
[25] A. Lawal, A. Shaari, R. Ahmed, L. S. Taura, *Curr. Appl. Phys.* **2018**, *18*, 567.
[26] F. Luckert, M. V. Yakushev, C. Faugeras, A. V. Karotki, A. V. Mudryi, R. W. Martin, *J. Appl. Phys.* **2012**, *111*, 093507.
[27] A. Stoliaroff, A. Lecomte, O. Rubel, S. Jobic, X. Zhang, C. Latouche, X. Rocquefelte, *ACS Appl. Energy Mater.* **2020**, *3*, 2496.
[28] D. H. Fabini, M. Koerner, R. Seshadri, *Chem. Mater.* **2019**, *31*, 1561.
[29] G. Zhang, A. Chaves, S. Huang, F. Wang, Q. Xing, T. Low, H. Yan, *Sci. Adv.* **2018**, *4*, eaap9977.
[30] M. Kuwata-Gonokami, in *Comprehensive Semiconductor Science and Technology*, Vol. *2* (Eds: P. Bhattacharya, R. Fornani, H. Kamimura), Elsevier, New York **2011**, pp. 213–255.
[31] J. C. Kim, D. R. Wake, J. P. Wolfe, *Phys. Rev. B* **1994**, *50*, 15099.
[32] H. D. Sun, T. Makino, Y. Segawa, M. Kawasaki, A. Ohtomo, K. Tamura, H. Koinuma, *Appl. Phys. Lett.* **2001**, *78*, 3385.
[33] N. Q. Liem, V. X. Quang, D. X. Thanh, J. I. Lee, D. Kim, *Solid State Commun.* **2001**, *117*, 255.
[34] G. Kuang, W. Gebhardt, E. Griebl, K. Sube, M. Kastner, M. Wörz, T. Reisinger, *Appl. Phys. Lett.* **1997**, *70*, 2717.
[35] A. Shongalova, M. R. Correia, B. Vermang, J. M. V. Cunha, P. M. P. Salomé, P. A. Fernandes, *MRS Commun.* **2018**, *8*, 865.
[36] P. Vidal-Fuentes, M. Guc, X. Alcobe, T. Jawhari, M. Placidi, A. Pérez-Rodríguez, E. Saucedo, V. I. Roca, *2D Mater.* **2019**, *6*, 045054.
[37] N. Fleck, T. D. C. Hobson, C. N. Savory, J. Buckeridge, T. D. Veal, M. R. Correia, D. O. Scanlon, K. Durose, F. Jäckel, *J. Mater. Chem. A* **2020**, *8*, 8337.
[38] T. D. C. Hobson, O. S. Hutter, M. Birkett, T. D. Veal, K. Durose, in *2018 IEEE 7th World Conf. Photovoltaic Energy Conversion (A Joint Conf. of 45th IEEE PVSC, 28th PVSEC and 34th EU PVSEC)*, IEEE, Piscataway, NJ **2018**, pp. 0818–0822, https://doi.org/10.1109/PVSC.2018.8547622.
[39] R. Kaupmees, M. Grossberg, M. Ney, A. Asaithambi, A. Lorke, J. Krustok, *Phys. Status Solidi RRL* **2020**, *14*, 1900355.
[40] J. Krustok, R. Kaupmees, R. Jaaniso, V. Kiisk, I. Sildos, B. Li, Y. Gong, *AIP Adv.* **2017**, *7*, 065005.
[41] Y. P. Varshni, *Physica* **1967**, *34*, 149.
[42] J. Krustok, H. Collan, K. Hjelt, *J. Appl. Phys.* **1997**, *81*, 1442.
[43] S. Rana, K. Awasthi, S. S. Bhosale, E. W.-G. Diau, N. Ohta, *J. Phys. Chem. C* **2019**, *123*, 19927.